The 27–28 October 1986 FIRE IFO Cirrus Case Study: Spectral Properties of Cirrus Clouds in the 8–12 μm Window

STEVEN A. ACKERMAN,* W. L. SMITH,* J. D. SPINHIRNE,+ AND H. E. REVERCOMB*

*Cooperative Institute for Meteorological Satellite Studies, Space Science and Engineering Center, University of Wisconsin-Madison, Madison, Wisconsin
+National Aeronautics and Space Administration, Goddard Space Flight Center, Greenbelt, Maryland

(Manuscript received 17 February 1989, in final form 12 June 1990)

ABSTRACT

Lidar and high spectral resolution infrared radiance observations taken on board the ER-2 on 28 October 1986 are used to study the radiative properties of cirrus cloud in the 8–12 μm window region. Measurements from the High-spectral resolution Interferometer Sounder (HIS) indicate that the spectral variation of the equivalent blackbody temperature across the window can be greater than 5°C for a given cirrus cloud. This difference is attributed to the presence of small particles.

A method for detecting cirrus clouds using 8 μm, 11 μm, and 12 μm bands is presented. The 8 μm band is centered on a weak water-vapor absorption line while the 11 μm and 12 μm bands are between absorption lines. The brightness temperature difference between the 8 and 11 μm bands is negative for clear regions, while for ice clouds it is positive. Differences in the 11 and 12 μm channels are positive, whether viewing a cirrus cloud or a clear region. Inclusion of the 8 μm channel therefore removes the ambiguity associated with the use of 11 and 12 μm channels alone. The method is based on the comparison of brightness temperatures observed in these three channels.

The HIS and lidar observations were combined to derive the spectral effective beam emissivity (ϵ) of the cirrus clouds. Fifty percent of clouds on this day displayed a spectral variation of ϵ from 2–10%. These differences, in conjunction with large differences in the HIS observed brightness temperatures, indicate that cirrus clouds cannot be considered gray in the 8–12 μm window region.

The derived spectral transmittance of the cloud is used to infer the effective radii of the particle size distribution, assuming ice spheres. For 28 October 1986 the effective radius of cirrus cloud particle size distribution (r_{eff}) was generally within the 30–40 μm range with 8% of the cases where $10 < r_{eff} < 30$ μm and 12% of the cases corresponding to $r_{eff} > 40$ μm.

1. Introduction

The 8–12 μm spectral region is an important atmospheric window for radiometric studies of the earth's surface and clouds. Selective gaseous absorption in this window occurs in the 9.6 μm ozone band with the remaining absorption dominated by water vapor. This spectral window is also very important for climate studies since most of the earth–atmosphere longwave radiative loss to space occurs in this spectral region. Cirrus clouds have a large impact on the attenuation of radiation in this atmospheric window region (Platt 1973; Liou 1974; Stephens 1980; Wu 1984). Understanding the interaction of cirrus clouds with the radiation field is critically important for climate studies and in interpreting satellite radiometric measurements. This understanding is hampered by the large variability of cirrus optical properties, making it difficult to determine their presence, let alone their radiative impact.

Corresponding author address: Dr. Steven A. Ackerman, Cooperative Institute for Meteorological Satellite Studies, University of Wisconsin–Madison, Madison, WI 53706

This study focuses on observations of the radiative properties of cirrus clouds within this window region. Lidar and radiometric observations are employed for detecting the presence of cirrus and describing their radiative properties. The instrumentation that achieved the spectral radiance observations used in the study is described. Results are presented for the 28 October 1986 FIRE case study day in terms of brightness temperature differences, cirrus effective emissivities and the gross microphysical characteristics of the observed clouds.

2. Instrumentation

During the First ISCCP Region Experiment (FIRE), simultaneous lidar and high spectral resolution infrared radiance observations of cirrus clouds were taken from the NASA ER-2. The radiometric observations were conducted with the High-spectral resolution Interferometer Sounder (HIS). The HIS (Smith et al. 1986) is a Michelson Interferometer with a spectral resolving power ($\lambda/\Delta\lambda$) of approximately 2000 covering the spectral range from 3.7–17.0 μm. The HIS spectra have

a resolution of approximately 0.5 cm^{-1} from 600–1100 cm^{-1} (9.1–16.7 μm), and 1.0 cm^{-1} resolution from 1100–2700 cm^{-1} (3.7–9.1 μm). The ground resolution of the HIS nadir observations is approximately 2 km from an ER-2 altitude of 19.8 km. Detection in each of three spectral bands is performed using liquid helium cooled arsenic doped silicon detectors contained in a single detector–dewar assembly. Three detector–filter systems are used to optimize the signal-to-noise ratio of the observations throughout the broad spectral region measured. High emissivity, temperature-controlled reference blackbodies are used for an absolute calibration. Each group of HIS interferograms consists of two cold blackbody views, two hot blackbody views, and six earth views for each scan direction of the mirror. The four blackbody views are used for the calibration of the six earth views. The noise equivalent temperature and calibration accuracy are both about 0.1°–0.2°C over much of the spectrum. A detailed description of the instrument and its calibration is given in Revercomb et al. (1988).

The Cloud and Aerosol Lidar (CALS) on board the ER-2 consists of a Nd:YAG laser that transmits polarized light at a frequency-doubled mode at 532 nm and at a rate of 5 Hz, or approximately every 41 meters along the flight line. CALS measures the total attenuated backscatter coefficient, $B'(Z)$, of the atmospheric constituents below the ER-2 as a function of height. To determine $B'(Z)$ the return power received by the lidar must be calibrated in terms of the backscatter coefficient and range. This calibration of the CALS is carried out for each shot profile using a vertical segment of the upper atmosphere where the backscatter coefficient for Rayleigh scattering is known. Final calibration constants are then derived from a large number of lidar shot profiles. Cloud top heights were derived in a manner described by Spinhirne and Hart (1990) for each lidar profile. For optically thin clouds, ground returns can be seen in the lidar shot profiles and are used to discriminate "thin" cirrus clouds from "thick" cirrus clouds. Cloud bases for the thin clouds were determined based on a simple threshold method. This threshold was also applied to the thick clouds although it is not representative of the actual cloud base. Cloud integrated attenuated backscatter, γ, corresponding to each HIS observation was determined by integrating the attenuated backscatter profiles throughout the depth of the cloud.

There were a total of 173 concurring HIS and CALS data points for the time period 1640–1820 UTC. The flight track of the ER-2 during this time covered south-central Wisconsin. A discussion of the synoptic conditions is given by Starr and Wylie (1990).

3. Data analysis

Figure 1 is an example of four HIS spectra (clear, altocumulus, and two cirrus) over the spectral range 8–13 μm observed during the 28 October FIRE case study day. While the HIS measures the radiance in the 9–10 μm band for retrieval of O_3, it has been omitted in Fig. 1. The individual gaseous absorption lines, primarily due to water vapor, are evident in the clear and low-level cloud cases (i.e., highest brightness temperatures) depicted in Fig. 1. The effect of the water-vapor continuum is seen as a trend of decreasing equivalent blackbody temperature with increasing wavelength in the 10–13 μm window. The high thick cirrus case also depicts a decreasing trend with a blackbody temperature difference of 5°C between wavelengths of 10 and 12 μm. This change is due to cloud radiative properties and is consistent with the absorption coefficient of ice ($\kappa = 4\pi n_i/\lambda$), which changes by a factor of 9 (Fig. 2) between these two wavelengths. The maximum change in the absorption coefficient of ice is between 10 and 11 μm, a feature consistent with the maximum changes in the equivalent blackbody temperatures of Fig. 1.

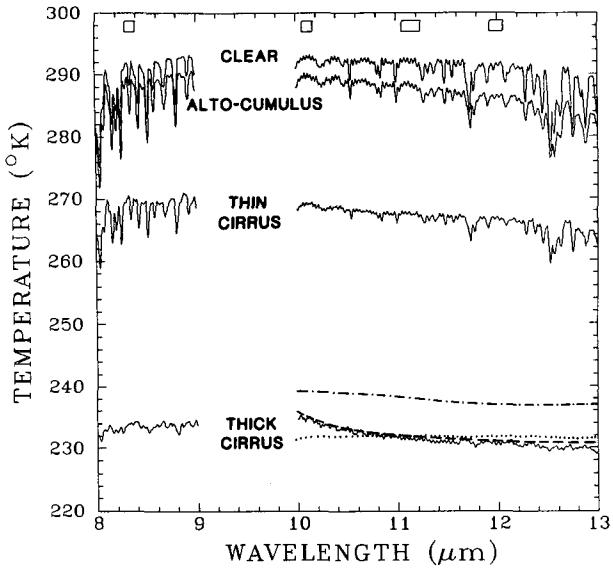

FIG. 1. Four HIS spectra (clear, altocumulus, and two cirrus) over the spectral range 8–13 μm observed during the 28 October FIRE case-study day. The dotted, dashed, and dot-dashed lines are theoretical calculations discussed in the text.

The spectral signature observed by the HIS (Fig. 1) is also related to the cloud particle size distribution. In Fig. 1, the dotted and dashed lines depict theoretical radiative transfer calculations using a 16 stream doubling–adding model and assuming a surface temperature of 279 K and a cloud top temperature of 230 K with an ice–liquid water path of 70 gm^{-2}. The cloud is assumed to have a lapse rate of 6°K km^{-1}, and gaseous absorption within the cloud is neglected. The cloud particles are assumed to be spheres with a gamma size distribution (Hansen and Travis 1974). The dashed-dotted curve in Fig. 1 assumes a cloud ice particle size distribution with an effective radius (defined as the ratio of the third moment of the size distribution

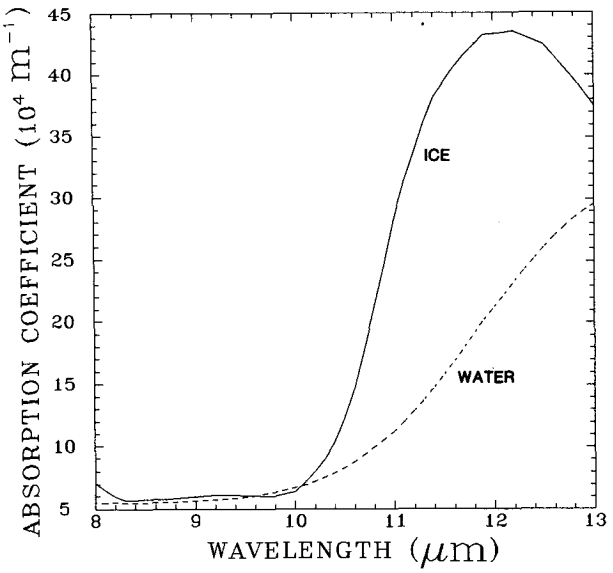

FIG. 2. The absorption coefficient of ice over the spectral range 8–13 μm.

to the second moment) of $r_{eff} = 25$ μm and a variance $b = 0.25$. The dashed curve assumes an ice particle size distribution of $r_{eff} = 13$ μm, $b = 0.25$. The dotted curve shows a water particle size distribution of $r_{eff} = 13$ μm, $b = 0.25$. These calculations show that the ice cloud with the smaller r_{eff} displays the spectral signature observed by the HIS, while the ice cloud with the larger r_{eff} displays little spectral variation in the equivalent blackbody temperature. These theoretical calculations demonstrate that the HIS observed spectral signature is related to the particle size and to the particle index of refraction.

Particle shape also plays a role in the spectral variability of the HIS observed radiances. Similar calculations assuming size distributions of cylindrical ice crystals yielded similar results: small particles are required for large brightness temperature differences across the window region. The r_{eff} used in this study corresponds to spherical ice particles that simulate the radiative features of the cloud within the spectral band considered. Ice clouds are not composed of spherical particles and thus the derived r_{eff} may not reproduce radiometric observations at wavelengths far from this region, such as the visible and near infrared.

a. Brightness temperature differences and cirrus cloud detection

To further investigate the spectral variation of the equivalent blackbody temperatures in the "window" region, four spectral bandwidths were considered: 8 μm (8.3–8.4), 10 μm (10.07–10.17), 11 μm (11.06–11.25), and 12 μm (11.93–12.06). These bandwidths are depicted at the top of Fig. 1 as boxes. The 10, 11, and 12 μm windows were chosen to minimize gaseous absorption effects. The 8 μm band was chosen to include the effects of a weak water-vapor absorption line. The mean brightness temperatures in these bands are referred to as BT_8, BT_{10}, BT_{11}, and BT_{12}. Figure 3 depicts brightness temperature differences for the 1700–1720 UTC time period (solid line is BT_{11}–BT_{12}, dot-dash line is BT_{10}–BT_{11}, and dotted line represents the BT_8–BT_{11}). Also shown at the bottom of the figure is the integrated cloud attenuated backscatter [$\gamma = \int_{Zb}^{Zt} \times B'(z)dz$] measured by the CALS. In addition, if the lidar receives a return signal from the ground, then an *s* is marked above the γ and is referred to as a *thin* cloud. An *x* denotes a *thick* cirrus, where no return signal from the ground was received. The CALS observations of this case study day are presented by Spinhirne and Hart (1990). The lidar indicated a thick cirrus cloud with a top between approximately 10–11 km during the period 1710–1715. Between 1707–1710 the lidar received signals from a cloud located between 7 and 11 km as well as from the surface. The lidar measurements also indicated the presence of a cloud near 4 km during the period 1718–1719. When the HIS was viewing a cirrus cloud, as determined from the CALS measurements, the three brightness temperature differences were positive, whether the cloud was thick or thin cirrus. In addition, for the cirrus clouds BT_{10}–BT_{11} and BT_8–BT_{11} were similar in magnitude and ranged from 1.5° to 7°C. The brightness temperature differences BT_{10}–BT_{11} and BT_8–BT_{11} are larger than BT_{11}–BT_{12}. For the cloud near 4 km the BT_{10}–BT_{11} tends to follow the BT_{11}–BT_{12}, varying between 1° and 2°C with BT_8–BT_{11} being slightly negative. In the cloud free case, BT_{11}–BT_{12} is also similar to the BT_{10}–BT_{11}, both being positive, while BT_8–BT_{11} is negative.

Differences in the brightness temperatures observed in these channels suggest a potentially useful technique for detecting the presence of cirrus clouds. The cloud-free regions have negative differences in BT_8–BT_{11} due to absorption by near surface water vapor, while cirrus clouds have positive differences owing to the optical properties of ice. This relationship is further demonstrated in Fig. 4, which is a scatter diagram of the BT_8–BT_{11} versus BT_{11}–BT_{12} for observations made during the period 1640–1820 UTC. Each symbol in Fig. 4 represents a range in altitude of the CALS measured maximum attenuated backscatter coefficient, $B'(Z)$. The solid triangles are CALS determined clear regions; one can see that a threshold of BT_8–$BT_{11} < -0.4$°C classifies all the cloud free regions correctly. This threshold may vary as a function of the water content of the atmosphere, but will always be negative. The negative values of BT_8–BT_{11}, appearing with midcloud altitude ranges of greater than 9.5 km, signify very thin cirrus clouds with thicknesses less than 200 m and an integrated backscatter of less than 0.005. The clouds with a maximum backscatter between 8.0 and 8.5 km tend to fall into two groups. In the first, BT_8–BT_{11} > BT_{11}–BT_{12} (points lying above the dotted line) and

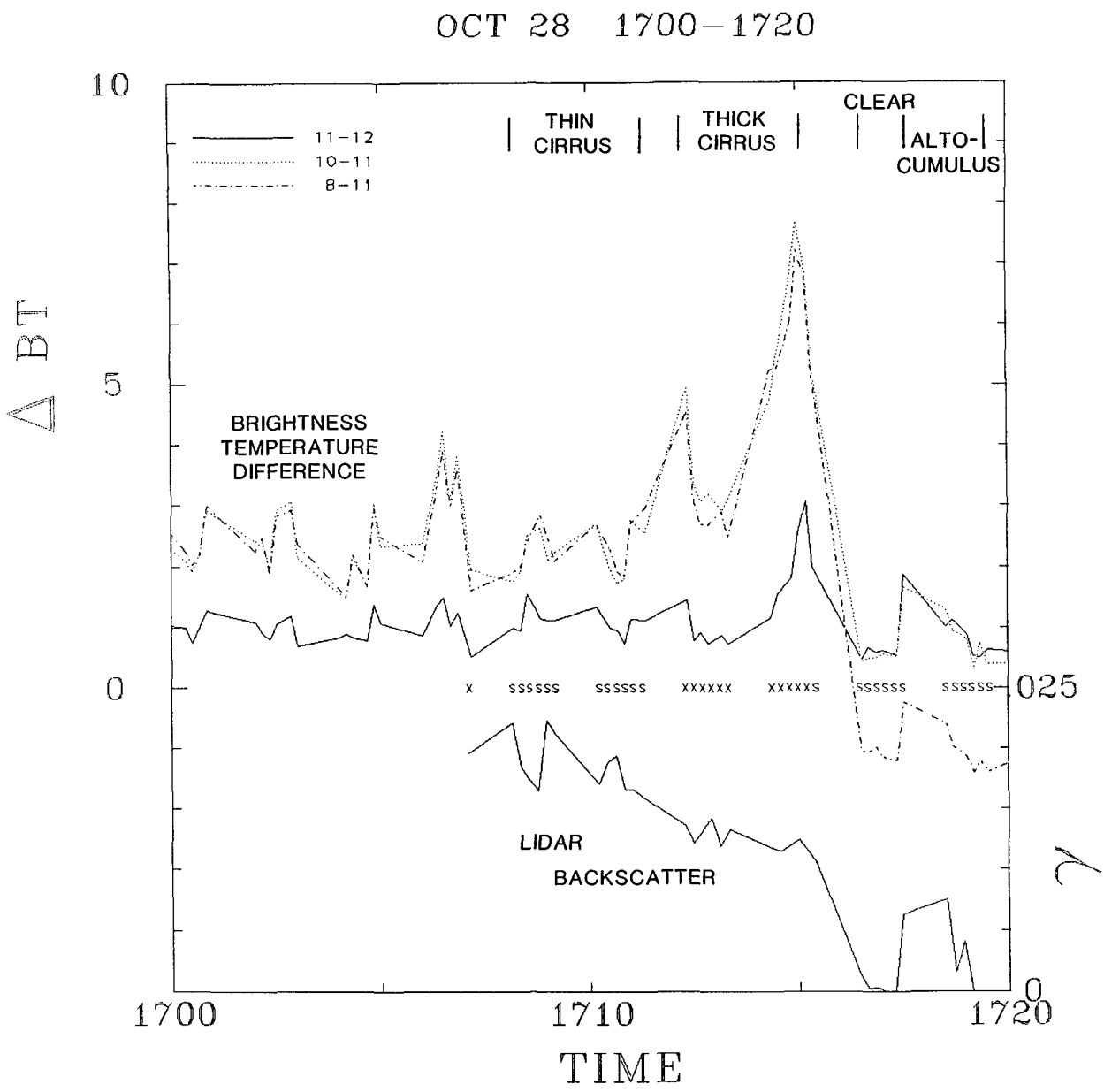

FIG. 3. Brightness temperature differences for the 1700–1720 UTC time period (solid line is BT_{11}–BT_{12}, dot-dash line is BT_{10}–BT_{11}, and dotted line represents the BT_8–BT_{11}). Also shown in the bottom of the figure is the integrated cloud attenuated backscatter measured by the CALS. The *s* denotes a thin cloud where the surface was seen by the lidar, while an *x* denotes a thick cloud where the lidar did not receive a signal from the surface.

represents the case of an ice cloud. The other group falls below the dotted line, such that BT_8–$BT_{11} < BT_{11}$–BT_{12}. This is representative of liquid-water clouds as the absorption coefficient for liquid water (Fig. 2) has a greater increase from 11 to 12 μm than from 8 to 11 μm. This results in the brightness temperature differences between 11 and 12 μm being greater than the brightness temperature differences between 8 and 11 μm in liquid-water clouds. Thus, the HIS and CALS combined observations indicate the presence of liquid water in a cloud between 8.0 and 8.5 km. This is consistent with the microphysical observations of Heymsfield and Miller (1990).

Bispectral measurements near 11 and 12 μm have been developed for remotely sensing the presence of cirrus clouds (e.g., Inoue 1985 and Prabhakara et al. 1988). A draw back of a bispectral technique at these wavelengths is that the brightness temperature differences between 11 and 12 μm are always positive, whether viewing a cloud or a clear region. Detecting

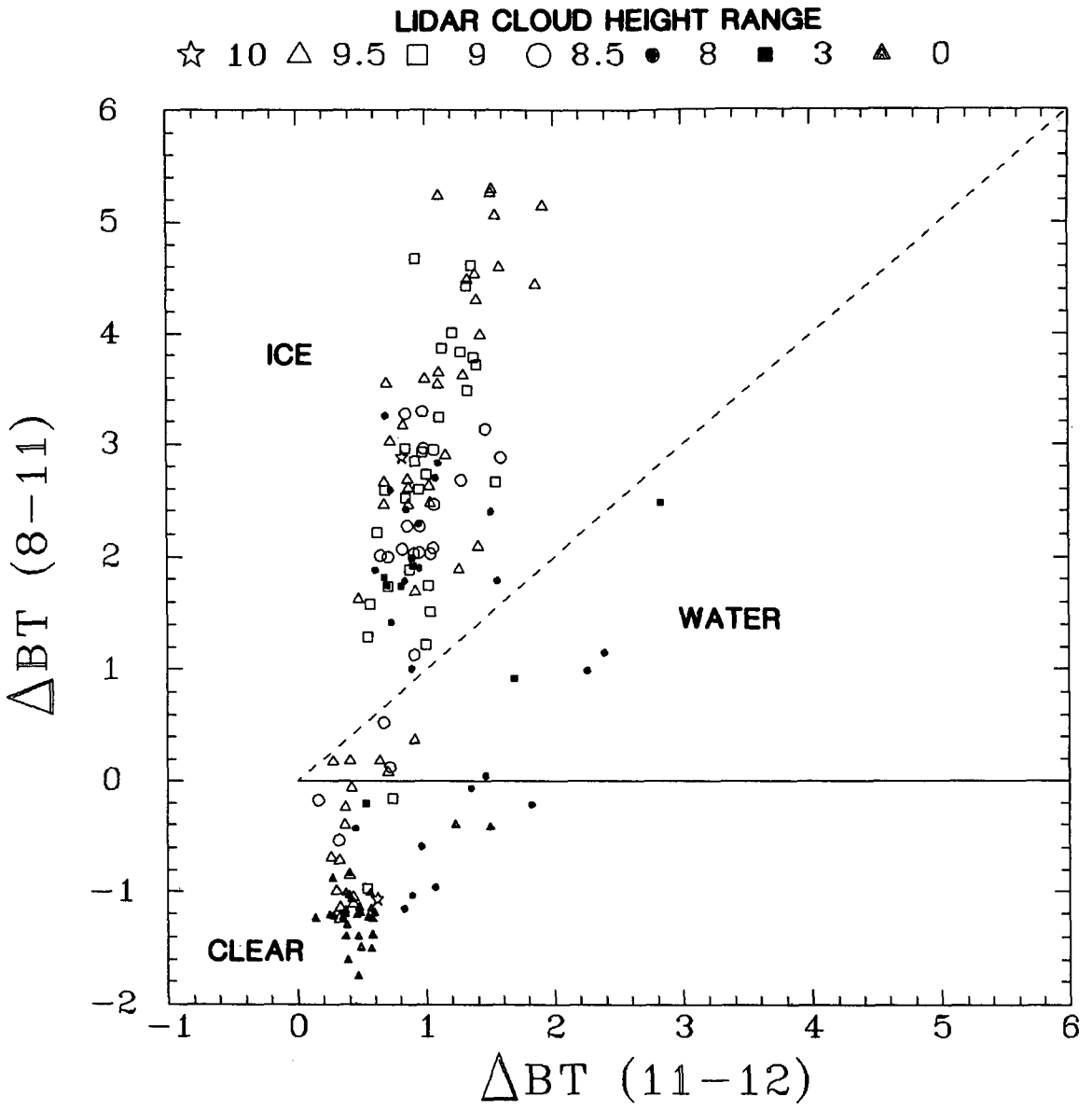

FIG. 4. Scatter diagram of the BT_8–BT_{11} versus BT_{11}–BT_{12}. Each symbol represents a range in altitude for which the CALS received the maximum $B'(Z)$.

cirrus using an 8 μm and an 11 μm channel is a more powerful method as water-vapor absorption results in a negative difference in the brightness temperatures, while this difference is generally positive for ice clouds. A three channel cloud detection technique using spectral measurements near 8, 11, and 12 μm poses the greatest potential for separating clear regions, cirrus clouds, and liquid water clouds, as demonstrated in Fig. 4.

b. Variability of cirrus emittance in the infrared window region

The equivalent blackbody radiative temperatures depicted in Figs. 1 and 3 indicate that cirrus clouds are not generally "gray bodies" in the 8–12 μm atmospheric window; the radiative properties of cirrus clouds may display a strong spectral dependency. In this section the CALS and HIS data are combined to derive the spectal effective beam emissivity (Platt and Stephens 1980) of cirrus clouds.

The radiances observed by the HIS can be expressed, neglecting scattering processes, as

$$I(Z_A) = B(T_S)\tau(Z_A, 0) + \int_0^{Z_A} B[T(Z)] \frac{d\tau(Z_A, Z)}{dz} dz \quad (1)$$

where $B(T_S)$ is Planck radiance of the surface, $\tau(Z_A,$

0) is the transmittance of the total atmosphere, and Z_A is the altitude of the aircraft (approximately 19.8 km). Separating (1) into above cloud (Z_A, Z_T), cloud (Z_T, Z_B), and below cloud (Z_B, Z_S) layers yields:

$$I(Z_A) = B(T_S)\tau(Z_A, 0) + \tau(Z_A, Z_B)\int_0^{Z_B} B[T(Z)]\frac{d\tau(Z_B, Z)}{dz}\,dz + \tau(Z_A, Z_T)\int_{Z_B}^{Z_T} B[T(Z)]\frac{d\tau(Z_T, Z)}{dz}\,dz + \int_{Z_T}^{Z_A} B[T(Z)]\frac{d\tau(Z_A, Z)}{dz}\,dz \quad (2)$$

where Z_B and Z_T are the height of cloud base and top respectively and are defined from the $B'(Z)$ profiles measured by the CALS (Spinhirne and Hart 1990). The temperature at the cloud boundaries are determined from temperature profiles measured by a nearby radiosonde. Denoting the radiance at cloud base as

$$I(Z_B) = B[T_S]\tau(Z_B, 0) + \int_0^{Z_B} B[T(Z)]\frac{d\tau(Z_B, Z)}{dz}\,dz \quad (3)$$

and using the mean value theorem to represent the mean cloud radiance as

$$\overline{B_C} = [1 - \tau(Z_T, Z_B)]^{-1} \times \int_{Z_B}^{Z_T} B[T(Z)]\frac{d\tau(Z_T, Z)}{dz}\,dz \quad (4)$$

the cloud layer transmittance is defined as

$$\tau(Z_T, Z_B) = \left[\frac{I(Z_A) - \int_{Z_T}^{Z_A} B[T(Z)]\frac{d\tau(Z_A, Z)}{dz}\,dz}{\tau(Z_A, Z_T)} - \overline{B_C}\right] \times [I(Z_B) - \overline{B_C}]^{-1}. \quad (5)$$

An initial spectral transmittance of the cloud is derived by first assuming a value for $\overline{B_C}$, in this case the Planck radiance at the midcloud temperature. The atmospheric transmittances above the cloud, $\tau(Z_A, Z_T)$, are computed based on the temperature and moisture profiles measured by a radiosonde launched at 1800 UTC at Greenbay WI. The above cloud contribution to the HIS observation,

$$\int_{Z_T}^{Z_A} B[T(Z)]\frac{d\tau(Z_A, Z)}{dz}\,dz,$$

is also theoretically determined. The clear-sky HIS radiances are used to define the spectral radiance at the cloud base after subtracting the effects of the above cloud atmosphere. The measured HIS spectra are then used to calculate the transmittance from (5). These first guess cloud spectral transmittances, $\tau(Z_T, Z_B)$, are then used to solve the integral in (4). Assuming that the Planckian emission is linear in optical depth,

$$B[T(Z)] = B[T(Z_T)] + \frac{B[T(Z_B)] - B[T(Z_T)]}{\ln\tau(Z_T, Z_B)}\ln\tau(Z_T, Z) \quad (6)$$

and

$$\int_{Z_B}^{Z_T} B[T(Z)]\frac{d\tau(Z_T, Z)}{dz}\,dz = B[T(Z_T)] - B[T(Z_B)]\tau(Z_T, Z_B) + \frac{B[T(Z_B)] - B[T(Z_T)]}{\ln\tau(Z_T, Z_B)}(\tau(Z_T, Z_B) - 1). \quad (7)$$

Equation (7) and the initial estimate of $\tau(Z_T, Z_B)$ are then used to calculate a corrected value of $\overline{B_C}$, and a new cloud transmittance is determined from (5). This iterative procedure is continued until the change in $\tau(Z_T, Z_B)$ is less than 0.003.

The results of this analysis are presented in terms of the spectral effective beam emissivity,

$$\epsilon(Z_T, Z_B) = 1 - \tau(Z_T, Z_B). \quad (8)$$

This effective emittance is larger than the true "absorption" emittance as it includes the effects of multiple scattering within the cloud and reflection at the cloud base (Platt and Stephens 1980). The difference between the effective emittance and the absorptance emittance is a function of the viewing angle, the particle size and shape, and the absorption component of the optical depth (δ_a). For nadir measurements at 11.5 μm (Platt

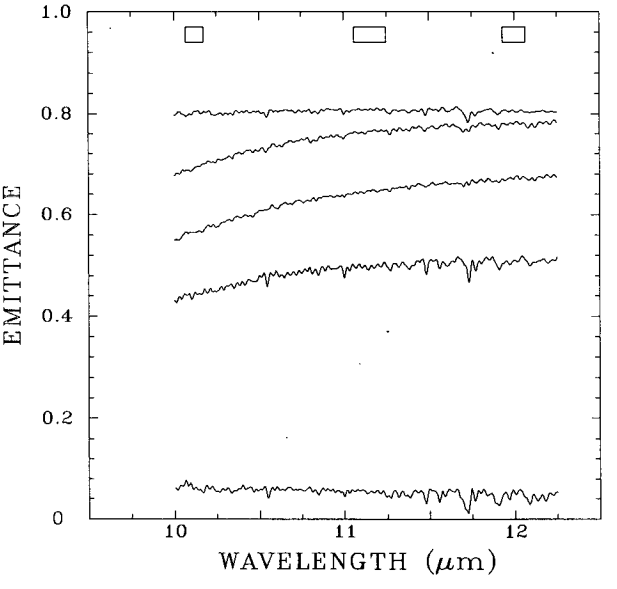

FIG. 5. Spectral effective beam emittance of five cirrus clouds.

and Stephens 1980) the difference is negligible for thin cloud, $\delta_a < 0.1$, and increases to a maximum of approximately 0.1 (15% error) at $\delta_a = 1.0$. The effective emissivity is used in this study to demonstrate the variability of cirrus clouds in the window region.

An example of the effective beam emissivity of five cirrus clouds is depicted in Fig. 5 as a function of wavelength. Two clouds appear gray with average beam emissivities of 0.8 and 0.06. The other three display a strong spectral variation, with a trend of increasing emissivity with increasing wavelength. These five examples are representative of the variability observed during FIRE. To investigate this spectral variation the four spectral regions discussed previously are analyzed in more detail. The frequency of occurrence of the spectrally-averaged beam emissivities for intervals of 0.1 is given in Fig. 6 for the 173 HIS and CALS coincident observations made on 28 October 1986. All four spectral regions have the greatest occurrence of effective beam emissivities between 0.4–0.9. Less than 30% of the cases studied have beam effective emissivities less than 0.4.

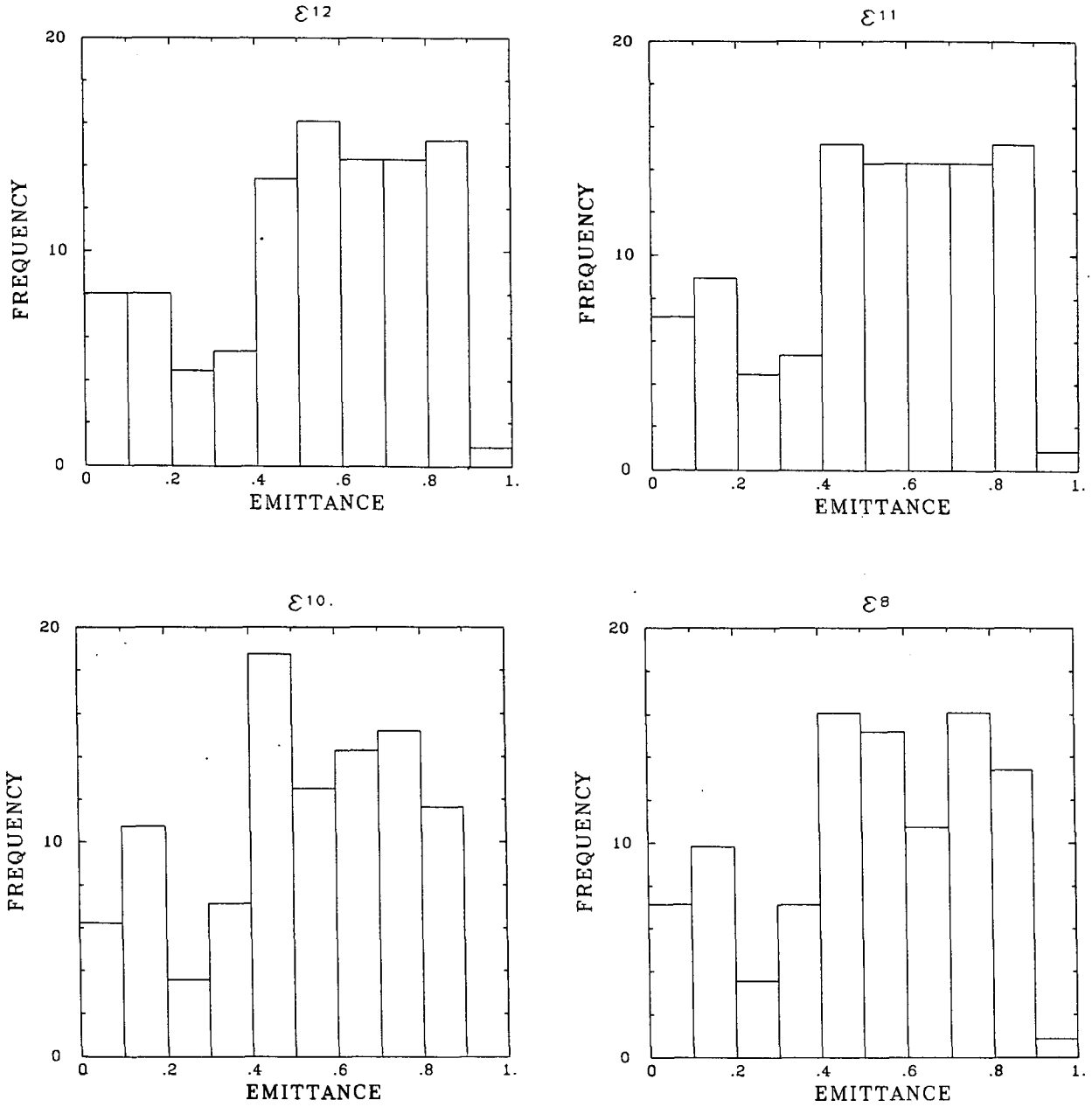

FIG. 6. The frequency of occurrence, in percent, of derived effective beam emissivities, at intervals of 0.1, for the four spectral bands discussed in the text.

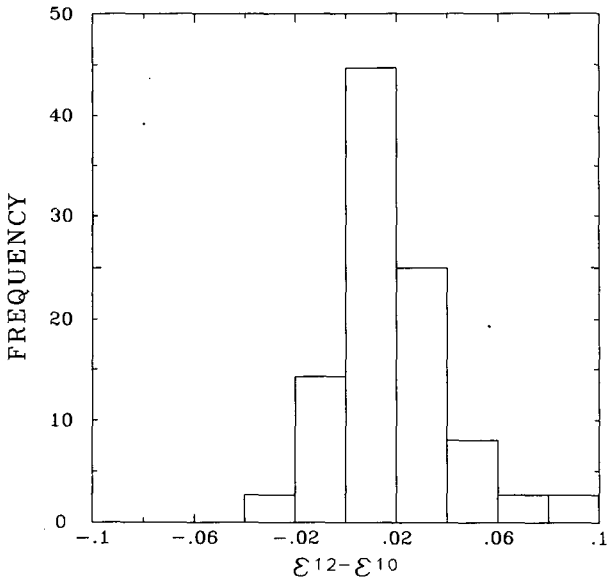

FIG. 7. A histogram of the percent occurrence of the difference in the effective beam emissivity at 12 and 10 μm.

To demonstrate the spectral variability of the emissivities, a histogram of the difference in the emissivity at 12 and 10 μm, $\Delta\epsilon^{12-10}$, is shown in Fig. 7. The histogram is skewed towards positive values of $\Delta\epsilon^{12-10}$, with approximately 50% of the clouds having $\Delta\epsilon^{12-10} > \pm 0.02$. The skew in the frequency distribution of $\Delta\epsilon^{12-10}$ results from the microphysical characteristics of the cloud as demonstrated by the theoretical calculations depicted in Figure 1. The skew in Fig. 7 and the brightness temperature differences depicted in Figs. 3 and 4 demonstrate that cirrus clouds cannot be considered gray in the 8–12 μm window region.

c. *HIS emissivity versus CALS integrated backscatter*

The relationship between the integrated attenuated backscatter of the CALS, $[\gamma = \int_{Zb}^{Zt} B'(z)dz]$ and the cloud emissivity in the 10 μm band (ϵ^{10}) is depicted in Fig. 8. Similar relationships are seen for emissivities in the other three bands. A large amount of scatter is exhibited in the relationship between γ and ϵ^{10} as the observations cover a variety of cloud types and the fields of view of the two instruments are not perfectly coregistered. The primary parameter that controls this variation is the midcloud temperature as demonstrated by Platt and Dilley (1981). The value of γ is a function of, first, the optical thickness of the cloud and second, the ratio of lidar backscatter to extinction. As the cloud thickness, and thus the emissivity, increases, the value of γ becomes determined primarily by the extinction

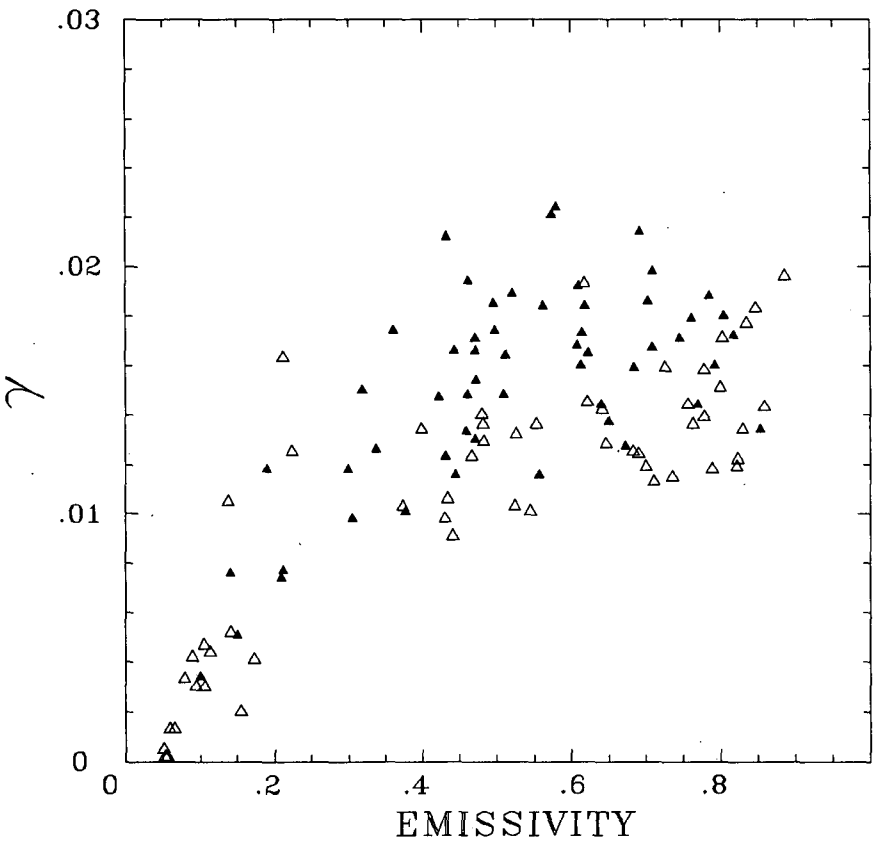

FIG. 8. The integrated backscatter of the CALS and the cloud beam emissivity in the 10 μm band. The solid triangles denote midcloud altitudes of less than 9 km, while the open triangles are for midcloud altitudes greater than 9 km.

to backscatter ratio. The extinction to backscatter ratio is a function of the particle size and shape, which are a function of the cloud temperature (Heymsfield and Platt 1984). To demonstrate this dependency, the values of γ and ϵ^{10} were grouped as a function of whether the midcloud altitude is above or below 9.5 km. The lower, warmer clouds are depicted in Fig. 8 as solid triangles while the higher, colder clouds are represented by open triangles. In general, the colder clouds tend to have a smaller value of γ for a given emissivity; however, in the present study there are too few cases to firmly establish this temperature dependency. A similar dependency on temperature was observed by Platt and Dilley (1981).

d. Inference of cloud microphysical properties

The dependency of the spectral variations in the HIS observed blackbody temperatures and effective emissivities to the effective radius of the size distribution is demonstrated in Fig. 9 where Mie calculations of the volume absorption coefficient (K_{abs}) are plotted as a function of r_{eff}. This relationship is depicted at the four window wavelengths discussed previously. The open symbols are for a size distribution where $b = 0.1$, while the solid symbols are for $b = 0.25$. The volume absorption coefficients at 8 and 10 μm are similar while the 11 and 12 μm K_{abs} tend to follow each other. K_{abs} is primarily determined by the effective radius of the distribution with the variance, b, playing a secondary role. This makes the effective radius a very useful parameter for radiative transfer calculations and parameterizations, as previously demonstrated by Hansen and Travis (1974) and by Ackerman and Stephens (1988). The utility of an effective radius in cloud microphysics is somewhat limited, as two size distributions with very different shapes can have the same effective radius. In addition, the effective radius assumes a distribution of ice spheres, while cirrus clouds are generally composed of nonspherical particles. The r_{eff} is still a useful parameter if it can simulate the radiative effects of nonspherical particles.

As the spectral structure in the 10–12 μm window is related to cloud particle size distribution, suggested by Figs. 1 and 9, high resolution spectral measurements from the HIS may be used to glean information regarding the variability of the bulk cirrus microphysical properties. For example, one may "best fit" the observed variation in the equivalent blackbody temperatures to theoretical calculations. This was done in Fig.

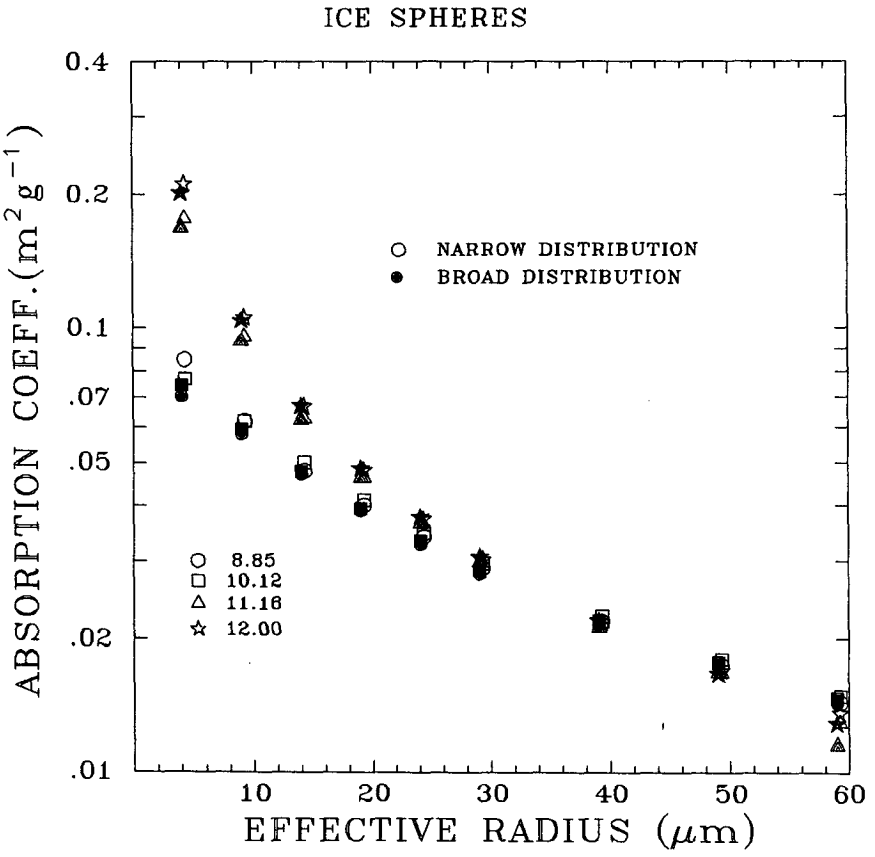

FIG. 9. Volume absorption coefficient [$K_{abs} = \pi \int n(r) r^2 Q_{abs} dr$] as a function of r_{eff} for four wavelengths as denoted in the legend. The open symbols are for a size distribution where $b = 0.1$, while the solid symbols are for $b = 0.25$.

1, in a comparison of HIS observations of thick cirrus clouds to model calculations. This comparison indicated that an effective radius of 13 μm would produce the spectral signature observed by the HIS. Another method to infer an appropriate effective radius, requiring fewer computations, is to neglect scattering. The spectral transmittance is then

$$\tau_\lambda = \exp[-K_{\lambda,\text{abs}}\text{IWC}(Z_T - Z_B)] \qquad (9)$$

where IWC is the ice water content of the cloud. Using the HIS transmittance measurements discussed in the previous section, the ratio of K_{10}/K_{12} can be derived by use of (9). The ratio of K_{10}/K_{12} from Mie calculations is shown in Fig. 10. The open symbols designate $b = 0.1$ while the solid symbols are for $b = 0.25$. For r_{eff} less than approximately 30 μm, $K_{10} < K_{12}$ and the ratio is smaller for larger b. This ratio goes to 1 for an r_{eff} between 30 and 40 μm, depending on the variance. This ratio is greater than 1 where r_{eff} is greater than approximately 40 μm.

The HIS derived parameter K_{10}/K_{12} can be used with Fig. 10 to estimate an effective radius. For the thick cirrus case presented in Fig. 1, this ratio method estimates an effective radius of between 15 and 20 μm. While this method is not as accurate as that used in Fig. 1, it can be used to distinguish between clouds consisting of large r_{eff} from those with small r_{eff}. The frequency of occurrence of the ratio of K at the 10 and 12 μm bands is depicted in Fig. 11 for this case study day. For 80% of the cases $0.85 \leq K_{10/12} \leq 1.0$, which would suggest effective radii between 20 and 40 μm. Eight percent of the cases have $0.65 < K_{10/12} < 0.85$, which corresponds to a range of r_{eff} between 10 and 20 μm, while 12% of the observations have $K_{10/12} > 1$, or an $r_{\text{eff}} > 40$ μm.

4. Conclusions

Measurements from the HIS radiometer and CALS lidar taken on board the ER-2 on 28 October 1986 are used to study the radiative properties of cirrus clouds in the 8–12 μm region. HIS observations demonstrate that cirrus clouds cannot be considered gray in this window region. The HIS measurements show that for a given cirrus cloud, spectral variations in equivalent blackbody temperatures can be greater than 5°C. Theoretical calculations indicate that the magnitude of the spectral variation in brightness temperature observed by the HIS is related to the effective radius of the size distribution of spherical ice particles (r_{eff}). The

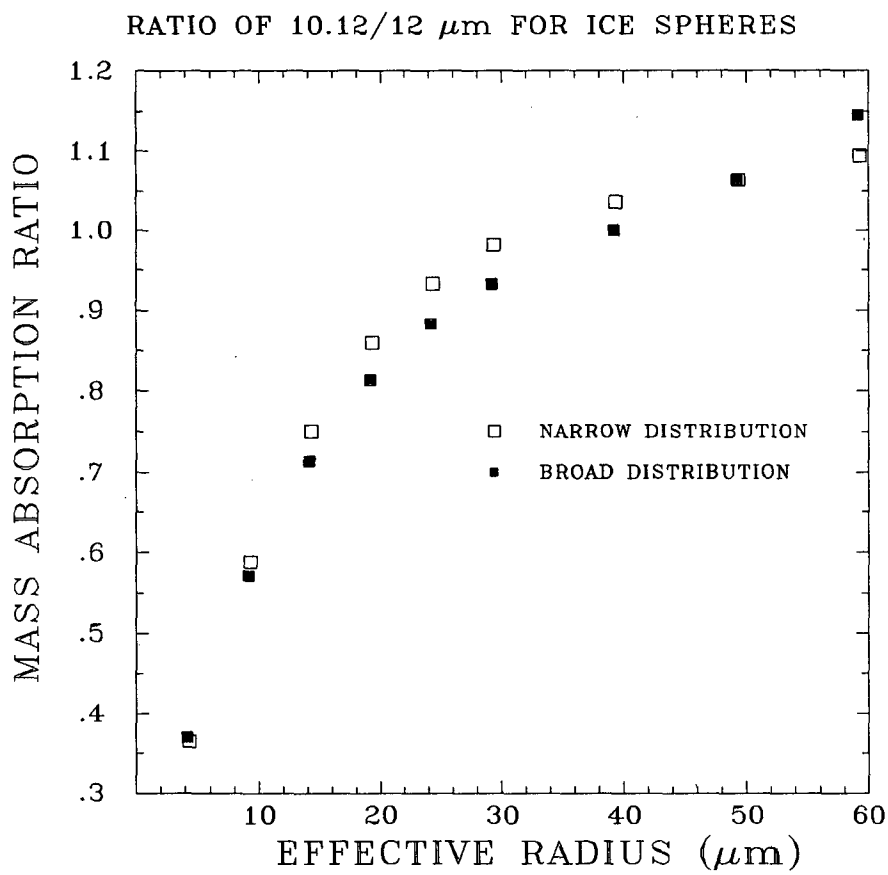

FIG. 10. The ratio of K_{abs} at 10 μm band to that of the 12 μm band. The open symbols are for a size distribution with $b = 0.1$, while the solid symbols are for $b = 0.25$.

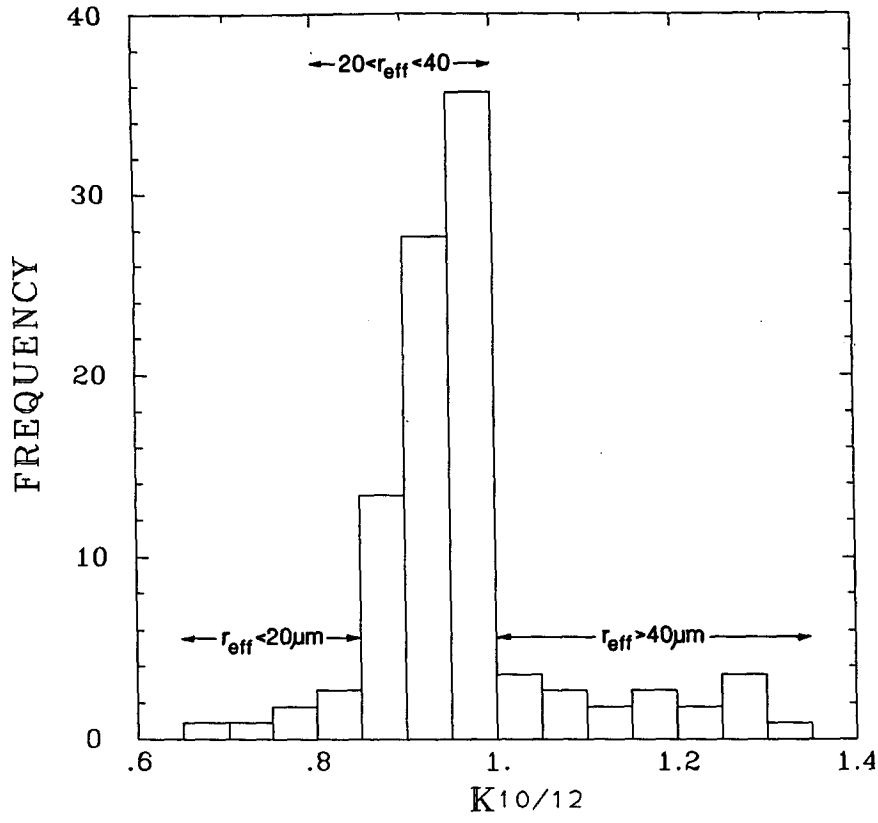

FIG. 11. The frequency of occurrence, in percent, of the ratio of K_{abs} at 10 and 12 μm on 28 October.

smaller r_{eff} are associated with larger brightness temperature differences.

A method of detecting cirrus clouds in terms of brightness temperature differences between 8, 11, and 12 μm bands is presented. The 8 μm band is centered on a weak water-vapor absorption line, while the 11 and 12 μm bands are between absorption lines. The brightness temperature difference between the 8 and 11 μm bands is negative for clear regions due to differences in water-vapor absorption, while for ice clouds it is positive. Differences in the 11 and 12 μm channels are positive, whether viewing a cirrus cloud or a clear region. The 8 μm channel, therefore, removes the ambiguity associated with the 11 and 12 μm channels. Inclusion of measurements in the 12 μm band distinguishes the cirrus cloud from lower layer liquid-water clouds.

The HIS and CALS observations were combined to derive the spectral effective beam emissivity of the cirrus clouds. The cirrus cloud beam emissivities were primarily limited to between 0.4–0.9, with less than 30% of the cases studied having beam emissivities less than 0.4. Fifty percent of the clouds on this day displayed a difference in the beam emissivity between 10 and 12 μm of greater than ± 0.02. The temperature dependency of the effective beam emissivity on the integrated cloud attenuated backscatter, γ, was similar to that observed by Platt and Dilley (1981): colder clouds had a smaller value of γ for a given emissivity.

The derived spectral transmittance of the cloud was used to infer a range in the effective radius, r_{eff}, of the particle size distribution. While the effective radius is only a gross representation of the microphysical properties of the cloud, it is extremely useful for radiative transfer calculations and parameterizations of cloud radiative properties. For 28 October 1986, the analysis of HIS observations in the 10 to 12 μm region indicates that effective radii of the cirrus clouds were generally within the 20–40 μm range with 8% of the cases being for $10 < r_{eff} < 20$ μm and 12% of the cases corresponding to $r_{eff} > 40$ μm. These radiometrically derived r_{eff} values are smaller than the in situ microphysical measurements made during this day (Heymsfield and Miller 1990). These differences may be attributed to the presence of small particles ($r < 25$ μm) not measured by the in situ observations, and/or due to the effect of particle shape on the radiative observations. The magnitude of this latter effect is presently being studied.

Acknowledgments. There are many people who, at some point, assisted in the analysis of the HIS data. We express our appreciation to them, and in particular to H. B. Howell, H.-L. Huang, R. O. Knuteson and

H. M. Woolf. Dennis Lhadka assisted with the lidar data image processing. This work was supported by the National Aeronautics and Space Administration under contract NAS1-18727 and the NASA Climate Research Office.

REFERENCES

Ackerman, S. A., and G. L. Stephens, 1988: The absorption of solar radiation by cloud droplets: an application of anomalous diffraction theory. *J. Atmos. Sci.*, **44,** 1574–1588.

Hansen, J. E., and L. D. Travis, 1974: Light scattering in planetary atmospheres. *Space Sci. Rev.*, **16,** 527–610.

Heymsfield, A. J., and C. M. R. Platt, 1984: A parameterization of the particle size spectrum of ice clouds in terms of the ambient temperature and the ice water content. *J. Atmos. Sci.*, **41,** 846–855.

——, K. M. Miller and J. D. Spinhirne, 1990: The 27–28 October 1986 FIRE cirrus case study: Cloud microstructure. *Mon. Wea. Rev.*, **118,** 2313–2328.

Jnoue, T., 1985: On the temperature and effective emissivity determination of semi-transparent cirrus clouds by bi-spetral measurements in the 10 μm window region. *J. Meter. Soc. Japan,* **63,** 88–89.

Liou, K. N., 1974: On the radiative properties of cirrus in the window region and their influence on remote sensing of the atmosphere. *J. Atmos. Sci.*, **31,** 522–532.

Platt, C. M. R., 1973: Lidar and radiometric observations of cirrus clouds. *J. Atmos. Sci.*, **30,** 1191–1204.

——, and G. L. Stephens, 1980: The interpretation of remotely sensed high cloud emittances. *J. Atmos. Sci.*, **37,** 2314–2322.

——, and A. C. Dilley, 1981: Remote sounding of high clouds. IV: Observed temperature variations in cirrus optical properties. *J. Atmos. Sci.*, **38,** 1069–1082.

Revercomb, H. E., H. Buijs, H. B. Howell, D. D. LaPorte, W. L. Smith and L. A. Sromovsky, 1988: Radiometric calibration of IR Fourier transform spectrometers: solution to a problem with the high-spectral resolution Interferometer Sounder. *Appl. Optics,* **27,** 3210–3218.

Smith, W. L., H. E. Revercomb, H. B. Howell, H. M. Woolf and D. D. LaPorte, 1986: The High resolution Interferometer Sounder (HIS). *CIMSS View,* Vol II, No. 3, University of Wisconsin.

Spinhirne, J. D., and W. D. Hart, 1990: The 27–28 October 1986 FIRE cirrus case study: ER-2 lidar and spectral radiometer cirrus observations. *Mon. Wea. Rev.*, **118,** 2329–2343.

Starr, D. O., and D. Wiley, 1990: The 27–28 October 1986 FIRE cirrus case study: meteorology and cloud fields. *Mon. Wea. Rev.*, **118,** 2259–2287. .

Stephens, G. L., 1980: Radiative properties of cirrus clouds in the infrared region. *J. Atmos. Sci.*, **37,** 435–445.

Wu, M. L. C., 1984: Radiative properties and emissivity parameterization of high level thin clouds. *J. Climate Appl. Meteor.*, **23,** 1138–1147.